

Theory and verification of moiré fringes for x-ray three-phase grating interferometer

Yu-Zheng Shan(单雨征), Yong-Shuai Ge(葛永帅), Jun Yang(杨君), Da-Yu Guo(郭大育), Xue-Bao Cai(蔡学宝), Xiao-Ke Liu(刘晓珂), Xiao-Wen Hou(侯晓文), and Jin-Chuan Guo(郭金川)

Citation: Chin. Phys. B, 2024, 33 (**5**): 056101. DOI: 10.1088/1674-1056/ad2bf5
Journal homepage: http://cpb.iphy.ac.cn; http://iopscience.iop.org/cpb

What follows is a list of articles you may be interested in

Surface structure modification of $ReSe_2$ nanosheets via carbon ion irradiation

Mei Qiao(乔梅), Tie-Jun Wang(王铁军), Yong Liu(刘泳), Tao Liu(刘涛), Shan Liu(刘珊), and Shi-Cai Xu(许士才)
Chin. Phys. B, 2023, 32 (**2**): 026101. DOI: 10.1088/1674-1056/ac7297

Equal compressibility structural phase transition of molybdenum at high pressure

Lun Xiong(熊伦), Bin Li(李斌), Fang Miao(苗芳), Qiang Li (李强), Guangping Chen(陈光平), Jinxia Zhu(竹锦霞), Yingchun Ding(丁迎春), and Duanwei He(贺端威)
Chin. Phys. B, 2022, 31 (**11**): 116102. DOI: 10.1088/1674-1056/ac673a

Pressure dependence of the thermal stability in $LiMn_2O_4$

Yan Zeng(曾彦), Hao Liang(梁浩), Shixue Guan(管诗雪), Junpu Wang(王俊普), Wenjia Liang(梁文嘉), Mengyang Huang(黄梦阳), and Fang Peng(彭放)
Chin. Phys. B, 2022, 31 (**1**): 016104. DOI: 10.1088/1674-1056/ac1932

Analytical solution of crystal diffraction intensity

Wan-Li Shang(尚万里), Ao Sun(孙奥), Hua-Bin Du(杜华冰), Guo-Hong Yang(杨国洪), Min-Xi Wei(韦敏习), Xu-Fei Xie(谢旭飞), Xing-Sen Che(车兴森), Li-Fei Hou(侯立飞), Wen-Hai Zhang(张文海), Miao Li(黎淼), Jun Shi(施军), Feng Wang(王峰), Hai-En He(何海恩), Jia-Min Yang(杨家敏), Shao-En Jiang(江少恩), and Bao-Han Zhang(张保汉)
Chin. Phys. B, 2021, 30 (**11**): 116101. DOI: 10.1088/1674-1056/ac0132

Doping effect on the structure and physical properties of quasi-one-dimensional compounds $Ba_9Co_3(Se_{1-x}S_x)_{15}$ (x = 0-0.2)

Lei Duan(段磊), Xian-Cheng Wang(望贤成), Jun Zhang(张俊), Jian-Fa Zhao(赵建发), Wen-Min Li(李文敏), Li-Peng Cao(曹立朋), Zhi-Wei Zhao(赵志伟), Changjiang Xiao(肖长江), Ying Ren(任瑛), Shun Wang(王顺), Jinlong Zhu(朱金龙), and Chang-Qing Jin(靳常青)
Chin. Phys. B, 2021, 30 (**10**): 106101. DOI: 10.1088/1674-1056/ac1f03

Theory and verification of moiré fringes for x-ray three-phase grating interferometer

Yu-Zheng Shan(单雨征)[1], Yong-Shuai Ge(葛永帅)[2,†], Jun Yang(杨君)[3], Da-Yu Guo(郭大育)[1], Xue-Bao Cai(蔡学宝)[4], Xiao-Ke Liu(刘晓珂)[5], Xiao-Wen Hou(侯晓文)[1,6], and Jin-Chuan Guo(郭金川)[1,‡]

[1] *Key Laboratory of Optoelectronic Devices and Systems of the Ministry of Education, Key Laboratory of Optoelectronic Devices and Systems of the Department of Education, Guangdong Province, College of Physics and Optoelectronic Engineering, Shenzhen University, Shenzhen* 518060, *China*

[2] *Research Center for Medical Artificial Intelligence, Shenzhen Institutes of Advanced Technology, Chinese Academy of Sciences, Shenzhen* 518055, *China*

[3] *Institute of Advanced Science Facilities, Shenzhen* 518107, *China*

[4] *Institute of Electronic Paper Displays, South China Academy of Advanced Optoelectronics, South China Normal University, Guangzhou* 510006, *China*

[5] *College of Biophotonics, South China Normal University, Guangzhou* 510631, *China*

[6] *MinFound Medical Systems Co., Ltd., Hangzhou* 310018, *China*

(Received 26 December 2023; revised manuscript received 16 February 2024; accepted manuscript online 22 February 2024)

Dual-phase and three-phase grating x-ray interference is a promising new technique for grating-based x-ray differential phase contrast imaging. Dual-phase grating interferometers have been relatively completely studied and discussed. In this paper, the corresponding imaging fringe formula of the three-phase grating interferometer is provided. At the same time, the similarities and differences between the three-phase grating interferometer and the dual-phase grating interferometer are investigated and verified, and that the three-phase grating interferometer can produce large-period moiré fringes without using the analyzing grating is demonstrated experimentally. Finally, a simple method of designing three-phase grating and multi-grating imaging systems from geometric optics based on the thin-lens theory of gratings is presented. These theoretical formulas and experimental results provide optimization tools for designing three-phase grating interferometer systems.

Keywords: x-ray phase contrast, phase grating, moiré fringe

PACS: 61.05.cp, 87.59.–e, 07.85.Fv, 41.50.+h **DOI:** 10.1088/1674-1056/ad2bf5

1. Introduction

Conventional x-ray absorption imaging uses the absorption coefficient or the difference in thickness among different parts of the object to create an image. This non-destructive imaging technique allows to access the information inside the object while preserving its structural integrity, thus being made have a wide range of applications in various fields such as medicine, security, and non-destructive testing.[1,2] In the hard x-ray band, the phase change of light element substance is more significant than the absorption change. Therefore, many researchers have conducted extensive researches on x-ray phase contrast imaging from the perspectives of imaging methods,[3–5] device fabrication,[6–8] and applications,[9–11] and many valuable advances have been made.

Depending on the principle of obtaining phase information, the existing phase contrast imaging methods are classified as five types: crystal interferometry,[12] propagation-based imaging,[13,14] diffraction-enhanced imaging,[15–17] grating-based phase-contrast imaging,[18,19] and coded aperture imaging.[20] The first two methods require high coherence of the light source, so they can only be implemented in synchrotron radiation or microfocus devices, making these two light source-based methods unsuitable for clinical or industrial applications, thus severely limiting the application of x-ray phase contrast imaging. Therefore, one of the most urgent issues in x-ray phase contrast imaging is to get rid of the dependence on synchrotron and microfocus spot x-rays and move from experimental application to clinical and routine applications. Grating-based phase-contrast imaging methods may resolve this issue. The x-ray grating phase-contrast imaging, also known as Talbot interferometry, uses the Talbot effect[21] to obtain the first-order phase shift information of x-rays passing through an object. Recently, grating-based phase-contrast x-ray interferometry has been developed and has achieved very promising results.[22–25] The Talbot–Lau interferometer is compatible with large focal spot x-ray tubes, which not only eliminates the inconvenience of using synchrotron radiation, but also solves the problem of insufficient flux of micro-focal spot x-ray sources. Dual-phase grating interferometer can produce large-period imaging fringes, which bring about a large field of view while reducing the sensitivity of the system, which is a contradiction that needs to be further resolved. To improve the sensitivity of grating interferometers, phase gratings with periods as small as a few micrometers or even submicrometers should be employed. However, hospital-grade imaging detectors that can be used in medical imaging have pixels of tens of micrometers. In order for a normal detector to detect fringes, an absorbing grating needs to be placed

†Corresponding author. E-mail: ys.ge@siat.ac.cn

‡Corresponding author. E-mail: jcguo@szu.edu.cn

© 2024 Chinese Physical Society and IOP Publishing Ltd

on the front surface of the detector.

However, the absorption grating blocks more than half of the x-rays that carry information about the object, and the only way to obtain the same information is to increase the radiation dose in the imaging study. At the same time, the fabrication challenge associated with absorption gratings is significantly greater than that associated with phase gratings, and this limitation in producing absorption gratings impedes the advancement of grating interferometer. Three-phase grating interferometry solves the problem about the dose inefficiencies of Talbot–Lau interferometry. One of the unique advantages of using three-phase gratings is that the hospital-grade imaging detectors can be used to resolve intensity fringes produced by fine-pitch phase gratings with no need to use absorption gratings. Thus, a greater intensity is transmitted through the interferometer and comparatively relaxed grating fabrication is required in the production process of gratings. In addition, the grating spacing is larger on a three-phase grating interferometer than on a dual-phase grating interferometer, thus making it easier to place samples, while the imaging field is much larger. For the above reasons and the fact that there is no systematic theoretical analysis of three-phase grating interferometers, we hereby give a more complete imaging theory for three-phase grating interferometer and experimentally verify it.

2. Imaging formula derivation

In this section, we will analyze and discuss the scalar diffraction calculation of x-rays in the system. First, we use Fresnel diffraction to derive the general expression of three-phase grating imaging.

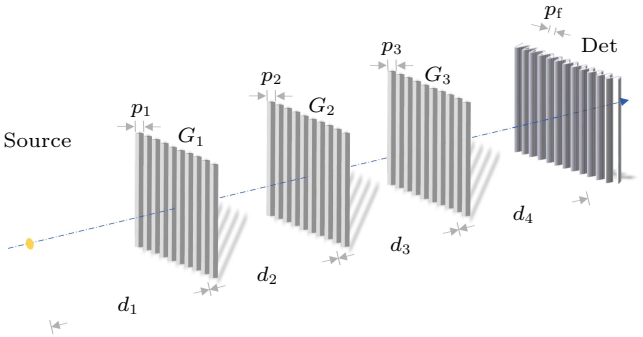


Fig. 1. Schematic diagram of three-phase grating interferometer, with G_1, G_2, and G_3 denoting phase gratings with periods of p_1, p_2, and p_3 respectively.

In Fig. 1, an ideal monochromatic spread source is placed at the far left of the optical path. Under the paraxial approximation, the complex amplitude distribution on the front surface of G_1 grating can be expressed as

$$\begin{aligned} U_1(x_1) &= \frac{U_0}{d_1}\exp(\mathrm{i}kr) \\ &= \frac{U_0}{d_1}\exp(\mathrm{i}kd_1)\times\exp\left[\frac{\mathrm{i}k}{2d_1}(x_1-x_\mathrm{s})^2\right], \end{aligned} \tag{1}$$

where $k=2\pi/\lambda$ is the wavenumber, U_0 is the light wave amplitude at the unit distance from the ideal light source, x_s is the horizontal coordinate of the source plane, and r_1 is the distance from the point on the source plane to the point on the G_1 grating plane. It is worth noting that in the x-ray imaging, the final physical quantity measured by the detector is the intensity of the x-rays, which needs to be modulo the complex amplitude and squared. For a phase grating with a one-dimensional duty cycle of 50%, the Fourier transform formula of its complex amplitude can be expressed as

$$T_1(x_1)=\sum_{n=-\infty}^{+\infty}a_n\exp\left(\frac{\mathrm{i}2\pi n x_1}{p_1}\right), \tag{2}$$

where n is the diffraction order of light. In derivation, we ignore the thickness of the grating. So, the convolution calculations of light waves and grating can be simplified into a multiplication calculation. After three Fresnel diffractions, the complex amplitude expression of x-ray in the detector plane can be expressed as

$$\begin{aligned} U_4(x_4) = {} & U_0\sum_n\sum_m\sum_q a_n b_m h_q \frac{\exp[\mathrm{i}k(L)]}{\sqrt{d_1d_2d_3d_4L}}\exp\left[\frac{\mathrm{i}\pi}{\lambda L}x_4^2\right] \\ & \times\exp\left[\mathrm{i}\pi\lambda\left(\frac{x_\mathrm{s}^2}{\lambda^2 d_1}-\frac{d_2}{M_1}\left(\frac{x_\mathrm{s}}{\lambda d_1}-\frac{n}{p_1}\right)^2\right.\right. \\ & -\frac{d_3}{M_2}\left(\frac{x_\mathrm{s}}{\lambda(d_1+d_2)}-\frac{n}{M_1p_1}-\frac{m}{p_2}\right)^2 \\ & \left.\left.-\frac{d_4}{M_3}\left(\frac{x_\mathrm{s}}{\lambda(d_1+d_2+d_3)}-\frac{n}{M_1M_2p_1}\right.\right.\right. \\ & \left.\left.\left.-\frac{m}{M_2p_2}-\frac{q}{p_3}\right)^2\right)\right] \\ & \times\exp\left[-\mathrm{i}2\pi\frac{x_4}{M_3}\left(\frac{x_\mathrm{s}}{\lambda(d_1+d_2+d_3)}\right.\right. \\ & \left.\left.-\frac{n}{M_1M_2p_1}-\frac{m}{M_2p_2}-\frac{q}{p_3}\right)\right], \end{aligned} \tag{3}$$

where $L=d_1+d_2+d_3+d_4$ is the total length of the system, n, m, and q are the diffraction orders of each grating, x_4 is the horizontal coordinate of the detector plane, and M_1, M_2, and M_3 are given as

$$\begin{aligned} M_1 &= \frac{d_1+d_2}{d_1}, \qquad M_2=\frac{d_1+d_2+d_3}{d_1+d_2}, \\ M_3 &= \frac{d_1+d_2+d_3+d_4}{d_1+d_2+d_3}. \end{aligned} \tag{4}$$

Please see Appendix A for detailed descriptions of the derivation process. The fundamental frequency term determines the frequency of the entire series, while the high-frequency component only determines the details of the series. Therefore, to calculate the period of light intensity, we must first determine its fundamental frequency terms.[26] If the three gratings have the same period, all of them are p_g. The conjugate coefficients of n, m, and q are set to n', m', q' respectively. When $n-n'=m-m'=q-q'=2$, we can obtain the

expression for the imaging fringe period of the three π phase gratings as follows:

$$p_{\mathrm{f}} = \frac{d_1+d_2+d_3+d_4}{d_2+d_3}\cdot\frac{p_{\mathrm{g}}}{2}. \tag{5}$$

For the $\pi/2$–π–$\pi/2$ phase grating system, when $n-n'=-1$, $m-m'=2$, and $q-q'=-1$, the imaging fringe obtains a maximum period, and the corresponding fringe period expression is given as

$$p_{\mathrm{f}} = \frac{d_1+d_2+d_3+d_4}{|d_2-d_3|}\cdot p_{\mathrm{g}}. \tag{6}$$

Equation (5) is fully consistent with previous results.[22,27,28] For Eq. (3), by considering the detector pixel size p_{del} and the width of the source σ, we can derive the detector plane light intensity expression as follows:

$$\begin{aligned}
I(x_4) = {} & \frac{U_0^2}{d_1d_2d_3d_4L}\sum_s\sum_r\sum_t \exp\left[\mathrm{i}2\pi\frac{x_4}{M_3}\left(\frac{s}{M_1M_2p_1}+\frac{r}{M_2p_2}+\frac{t}{p_3}\right)\right] \\
& \times C_s\left(\frac{d_2M_1M_2^2M_3+d_3M_2M_3+d_4+d_3M_1M_2M_3\frac{p_1}{p_2}\frac{s}{r}+d_4M_1\left(\frac{p_1}{p_2}\frac{r}{s}+M_2\frac{p_1}{p_2}\frac{t}{s}\right)}{M_1^2M_2^2M_3},\lambda,p_1,\phi_1\right) \\
& \times C_r\left(\frac{d_3M_2M_3+d_4+d_3M_3\frac{M_2}{M_1}\frac{p_2}{p_1}\frac{s}{r}+d_4\frac{1}{M_1}\frac{p_2}{p_1}\frac{s}{r}+d_4M_2\frac{p_2}{p_3}\frac{t}{r}}{M_2^2M_3},\lambda,p_2,\phi_2\right) \\
& \times C_t\left(\frac{d_4+d_4\frac{1}{M_1M_2}\frac{p_3}{p_1}\frac{s}{t}+d_4\frac{1}{M_2}\frac{p_3}{p_2}\frac{r}{t}}{M_3},\lambda,p_3,\phi_3\right) \\
& \times \exp\left[\mathrm{i}2\pi x_{\mathrm{s}}\left[\frac{d_2}{M_1}\frac{s}{d_1p_1}+\frac{d_3}{M_2}\frac{1}{d_1+d_2}\left(\frac{s}{M_1p_1}+\frac{r}{p_2}\right)+\frac{d_4}{L}\left(\frac{s}{M_1M_2p_1}+\frac{r}{M_2p_2}+\frac{t}{p_3}\right)\right]\right] \\
& \times \mathrm{sinc}\left[\left(\frac{d_2}{M_1}\frac{s}{d_1p_1}+\frac{d_3}{M_2}\frac{1}{d_1+d_2}\left(\frac{s}{M_1p_1}+\frac{r}{p_2}\right)+\frac{d_4}{M_3}\frac{1}{d_1+d_2+d_3}\left(\frac{s}{M_1M_2p_1}+\frac{r}{M_2p_2}+\frac{t}{p_3}\right)\right)\sigma\right] \\
& \times \mathrm{sinc}\left[\frac{p_{\mathrm{del}}}{M_3}\left(\frac{s}{M_1M_2p_1}+\frac{r}{M_2p_2}+\frac{t}{p_3}\right)\right],
\end{aligned} \tag{7}$$

where s, r, and t denote the difference of the conjugate diffraction orders of each grating. So far, we have obtained the general expression for the complex amplitude distribution of the optical field of the three-phase grating interferometer under extended source illumination with deviation from the source. The detailed derivation procedure may be found from Appendix A.

3. Relation between three-phase grating system and dual-phase grating system

In comparison with dual-phase grating imaging, three-phase phase grating imaging has only one additional phase grating. Therefore, we suspect that the imaging formula of a three-phase grating system must have some relationship with the imaging formula of a dual-phase grating system, rather than a mutually unrelated and sharply opposed relationship. According to Fourier optics and light diffraction, most of the energy of a light wave is concentrated in the diffracted light of the lower order. The outline of the image is determined by the lower-order diffracted light, while the higher-order diffracted light, which contains less energy, only determines the details of the image. In the next calculation, we ignore the details of the image and only care about the period of the image, so we can take only ±1 level of diffracted light (for $\pi/2$ we need to take level 0 and ±1). When $l=0$, the function $C_l=1$. C_l is an odd function when $4\pi\lambda d/p_{\mathrm{g}}^2$ is taken as an integer, and an even function when $4\pi\lambda d/p_{\mathrm{g}}^2$ is not an integer. In the actual experiment, we cannot make $4\pi\lambda d/p_{\mathrm{g}}^2$ an integer, so in the next calculation we will treat C_l as an even function. The expression for the light intensity in the detector plane can then be rewritten as

$$\begin{aligned}
I(x_4) = {} & \frac{2U_0}{d_1d_2d_3d_4L}\cos\left[2\pi\frac{x_4}{M_3}\left(\frac{2}{M_2p_2}+\frac{-2}{p_3}\right)+2\pi x_{\mathrm{s}}\varphi_1\right]\left[-2\frac{(-1)^{\delta_{2,23}}}{\pi}\sin\left(\frac{4\pi\lambda}{p_2^2}\frac{(d_1+d_2)(d_3+d_4)-d_4(d_1+d_2)\frac{p_2}{p_3}}{L}\right)\right] \\
& \times\left[2\frac{(-1)^{\delta_{3,23}}}{\pi}\sin\left(\frac{4\pi\lambda}{p_3^2}\frac{(d_1+d_2+d_3)d_4-d_4(d_1+d_2)\frac{p_3}{p_2}}{L}\right)\right]+\frac{2U_0}{d_1d_2d_3d_4L}\cos\left[2\pi\frac{x_4}{M_3}\left(\frac{2}{M_1M_2p_1}+\frac{-2}{p_3}\right)+2\pi x_{\mathrm{s}}\varphi_2\right]
\end{aligned}$$

$$\times\left[-2\frac{(-1)^{\delta_{1,13}}}{\pi}\sin\left(\frac{4\pi\lambda}{p_1^2}\frac{d_1(d_2+d_3+d_4)-d_1d_4\dfrac{p_1}{p_3}}{L}\right)\right]$$
$$\times\left[-2\frac{(-1)^{\delta_{3,13}}}{-\pi}\sin\left(\frac{4\pi\lambda}{p_3^2}\frac{(d_1+d_2+d_3)d_4-d_1d_4\dfrac{p_3}{p_1}}{L}\right)\right]+\frac{2U_0}{d_1d_2d_3d_4L}\cos\left[2\pi\frac{x_4}{M_3}\left(\frac{2}{M_1M_2p_1}+\frac{-2}{M_2p_2}\right)+2\pi x_s\varphi_3\right]$$
$$\times\left[-2\frac{(-1)^{\delta_{1,12}}}{\pi}\sin\left(\frac{4\pi\lambda}{p_1^2}\frac{d_1(d_2+d_3+d_4)-d_1(d_3+d_4)\dfrac{p_1}{p_2}}{L}\right)\right]$$
$$\times\left[-2\frac{(-1)^{\delta_{2,12}}}{-\pi}\sin\left(\frac{4\pi\lambda}{p_2^2}\frac{(d_1+d_2)(d_3+d_4)-d_1(d_3+d_4)\dfrac{p_2}{p_1}}{L}\right)\right], \tag{8}$$

where

$$\varphi_1 = \frac{d_3}{d_1+d_2+d_3}\frac{2}{p_2}+\frac{d_4}{L}\left(\frac{2}{M_2p_2}+\frac{-2}{p_3}\right),$$
$$\varphi_2 = \frac{d_2}{d_1+d_2}\frac{2}{p_1}+\frac{d_3}{d_1+d_2+d_3}\frac{2}{M_1p_1}+\frac{d_4}{L}\left(\frac{2}{M_1M_2p_2}+\frac{-2}{p_3}\right),$$
$$\varphi_3 = \frac{d_2}{d_1+d_2}\frac{2}{p_1}+\frac{d_3}{d_1+d_2+d_3}\left(\frac{2}{M_1p_1}+\frac{-2}{p_2}\right)+\frac{d_4}{L}\left(\frac{2}{M_1M_2p_2}+\frac{-2}{M_2p_2}\right).$$

When the above equation and the imaging equation for a dual-phase grating interferometer system are compared, we notice a striking similarity. We believe that one three-phase grating interferometer is equivalent to three dual-phase grating interferometers. The above equation can be expressed as

$$I_{G_1G_2G_3} = I_{G_1G_2}+I_{G_2G_3}+I_{G_1G_3}. \tag{9}$$

For a three-phase grating imaging system, if only G_3 is removed without changing any other parameters, it degenerates into a dual-phase grating imaging system, and the distance from G_2 to the detector is d_3+d_4, then the light intensity distribution of the system on the detector plane can be expressed as

$$I_{G_1G_2}(x_3) = \sum_n\sum_m\sum_{n'}\sum_{m'}\frac{U_0^2a_nb_ma_{n'}b_{m'}}{d_1d_2(d_3+d_4)L}\times\exp\left[\mathrm{i}2\pi\frac{(d_1+d_2)}{L}\left(\frac{n-n'}{M_1p_1}+\frac{m-m'}{p_2}\right)\right]\times\exp\left[\mathrm{i}\pi\lambda\frac{d_2}{M_1}\left(\frac{n'^2-n^2}{p_1^2}+\frac{2x_s(n-n')}{\lambda d_1p_1}\right)\right]\times\exp\left[\mathrm{i}\pi\lambda\frac{(d_1+d_2)(d_3+d_4)}{L}\times\left[\left(\frac{n'}{M_1p_1}+\frac{m'}{p_2}\right)^2-\left(\frac{n}{M_1p_1}+\frac{m}{p_2}\right)^2+\frac{2x_s}{(d_1+d_2)\lambda}\left(\frac{n-n'}{M_1p_1}+\frac{m-m'}{p_2}\right)\right]\right]. \tag{10}$$

Assuming that the three gratings all have the same period, p_g , and all of the phase differences are π, the fringe period of the imaging system can be expressed as

$$p_{f,G_1G_2} = \frac{L}{d_2}\cdot\frac{p_g}{2}. \tag{11}$$

Similarly, for a three-phase grating imaging system, only G_1 is removed without changing any parameter. In this case, the distance between the light source and the first grating becomes d_1+d_2, and the fringe period of the imaging system is given as

$$p_{f,G_2G_3} = \frac{L}{d_3}\cdot\frac{p_g}{2}. \tag{12}$$

Finally, by removing G_2 without changing any other parameters, the distance between the two gratings becomes d_2+d_3, and the fringe period of the imaging system becomes

$$p_{f,G_1G_3} = \frac{L}{d_2+d_3}\cdot\frac{p_g}{2}. \tag{13}$$

Next, we run simulations in MATLAB by using the above-derived equations, and the simulation results are as follows: $d_1=d_4=80$ cm, $d_2=d_3=3.679$ cm, and the grating period is 2.86 μm. The operating voltage of the grating is 17 keV, which corresponds to a light wavelength of 0.073 nm and the light source size of 5 μm.

When comparing Fig. 2(a) with Fig. 2(c), the fringe periods and contrasts of the two images are the same, indicating that without changing other conditions, the fringe images obtained after only removing G_1 grating and only removing G_3 grating are the same, which once again verifies the hypothesis of the principle of light path reversibility. At the same time, figure 2(d) shows that the fringe periods of the two simulated images are the same. By comparing Eqs. (5), (12), and (13), with Fig. 2(d), we believe that the three-phase grating image fringe consists of two parts. The first part is the small period fringe formed by the G_1G_3 gratings. Observing the imaging fringe period formula, we can find that the dual-phase grating imaging system composed of G_1G_3 gratings and

the three-phase grating system composed of $G_1G_2G_3$ gratings have the same imaging fringe period when the system length is the same; the second part is the large fringe formed by G_1G_2 gratings and G_2G_3 gratings. The space between its gratings is only half that of G_1G_3, and its fringe periods are twice that of the G_1G_3 grating fringe period, which is consistent with the result from the equation.

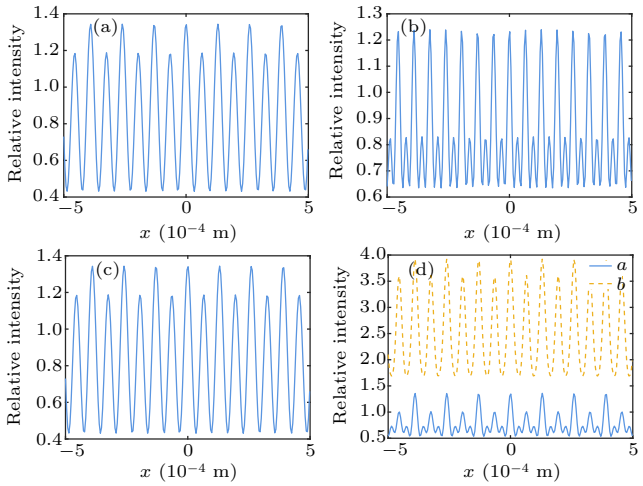


Fig. 2. (a)–(c) Simulation results of imaging fringes with zero phase difference of three gratings. (d) Curve "a" denotes the imaging fringe of three grating systems with the same configuration and curve "b" refer to the result of the algebraic addition of light intensities in panels (a)–(c).

After calculation and analysis, we can conclude that when the three grating periods are the same, the imaging formula of the three-phase grating interferometer can be converted into the imaging formula of the dual-phase grating under certain conditions, and the dual-phase grating imaging is a special case of the three-phase grating interferometer. For Eq. (8), when $d_1 = d_4$, $d_2 = d_3$, the period $p_{G_1G_2} = p_{G_2G_3}$. While in a practical experiment, we obviously cannot guarantee that d_2 is strictly the same as d_3, which would result in a difference between the two: $p_{G_1G_2} = p_{G_2G_3} + \Delta f$. Therefore, equation (8) can be expressed as

$$\begin{aligned} I(x_4) = {} & \frac{2U_0(-1)^{\delta}}{d_1d_2d_3d_4L}\frac{4}{\pi^2} \\ & \times \sin\left[\frac{4\pi\lambda}{p^2}\frac{(d_1+d_2)(d_3+d_4)-(d_1+d_2)d_4}{L}\right] \\ & \times \sin\left[\frac{4\pi\lambda}{p^2}\frac{(d_1+d_2+d_3)d_4-(d_1+d_2)d_4}{L}\right] \\ & \times 2\cos\left[\pi x_4(2f+\Delta f)\right. \\ & \left. + \frac{2\pi x_s}{p}\left(\frac{d_1d_3}{L}-\frac{(d_2+d_3)d_4}{(d_1+d_2+d_3)L}\right)\right] \\ & \times \cos\left[\pi x_4\Delta f + \frac{2\pi x_s}{p}\frac{d_3-d_2}{L}\right] + I_{G_1G_3}. \end{aligned} \tag{14}$$

In experiment, we have found that Δf is related not only to the length of the system but also to factors such as the direction of the grating fringes and the parallelism between the gratings.

4. Experimental setup, results, and discussion

4.1. Experimental setup

As shown in Fig. 3, we design a three-phase grating interferometer and verify it on a laboratory x-ray phase contrast imaging platform. For the microfocal spot source, the operating voltage and current of its light source are 40 keV and 180 μA, respectively, with a 100.00-s exposure time for each phase step. In addition, a 0.03-mm piece of Mo is placed on the light source to effectively filter the light source energy spectrum so that it can match the phase grating requirement. The detector active area is 38.75 mm×27.75 mm and the pixel size is 4.6 μm. The three π phase grating periods are all 2.86 μm with a duty cycle of 50%. The specific distance parameters of the system are as follows: the distance from light source to grating G_1 $d_1 = 98.024$ cm, the distance from grating G_1 to grating G_2 $d_2 = 4.226$ cm, the distance of grating G_2 to grating G_3 $d_3 = 4.226$ cm and the distance between grating G_3 and the detector $d_4 = 98.024$ cm. We use this system to verify the grating imaging fringe period theory and the connection and difference theory between three-phase grating interferometer and dual-phase grating interferometer.



Fig. 3. Physical diagram of experimental setup.

4.2. Results and discussion

We first take a set of fringe images without placing the object. As shown in Fig. 4(a), the captured image consists of two sets of fringes with different contrast, and the fringe period is approximately 67.24 μm, which is consistent with the theoretical value of 69.20 μm obtained from Eq. (5).

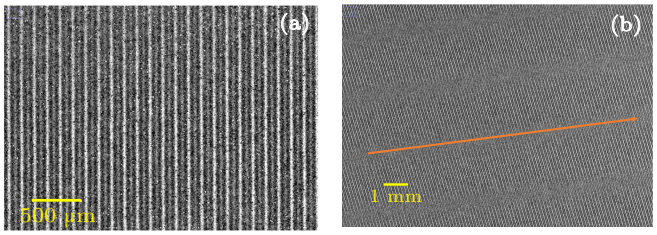


Fig. 4. Fringe image formed by three-phase grating interferometer for (a) placing no object and (b) fringe image.

Figure 4(b) shows another set of fringe images taken by rotating the gratings in the plane perpendicular to the optical axis. We observe both diffraction fringes and moiré fringes.

The period of the moiré fringes is about 7.8 mm. We now successfully produce large period moiré fringes without using an analyzing grating with our three-phase grating interferometer systems.

Some theoretical analysis and experimental verification are performed on the appearance of moiré fringes in a three-phase gratings interferometer. The results show that the direction and period of the large fringe change as G_2 is rotated in a specific range, and the moiré fringe rotates 12° for each 0.02° rotation of the G_2 grating. For our system, the range is roughly 0° with the grating perfectly parallel to the position of ±0.43°. While the amount of change in the direction of the large fringes due to the rotation of G_3 only is much smaller than that of G_2. Due to the symmetry of the system and the principle of reversibility of the optical path, we believe that rotating G_1 grating has the same effect as rotating G_3 grating. From previous analysis of the connection between the three-phase grating interferometer and the dual-phase grating interferometer, we believe that the interaction between the G_1 grating and G_2 grating creates a set of diffraction moiré fringes on the detector plane, while the interaction between the G_2 grating and G_3 grating also creates a set of diffraction moiré fringes on the detector plane. Since the three gratings have the same period and are very close to each other, the two sets of diffraction moiré fringes should have approximately the same period. The fringes we observed are the superposition of the light intensities of these two diffraction moiré fringes of similar periods on the detector plane. Only the G_2 grating is involved in the formation of both diffraction moiré fringes, while the G_1 grating and G_3 grating are only involved in the formation of one diffraction moiré fringe. As a result, the G_2 grating exhibits much higher sensitivity in generating the large fringe than the G_1 grating and G_3 grating. We establish a Cartesian coordinate system with the direction of the G_2 grating as the y axis, and set the deflection angle of the G_1 grating with respect to the y axis as θ_1 and the deflection angle of the G_3 grating with respect to the y axis as θ_2. When $p_1 = p_2 = p_3 = p$, $\theta_1 = \theta_2 = |\theta|$, the moiré fringe width can be expressed as

$$w = \frac{p}{\theta\left(|\theta_2 - \theta_1|\right)}. \tag{15}$$

When θ is within ±4°, the moiré fringe formed can reach the millimeter level, which is consistent with the phenomenon we observed in the experiment. In addition, departing from diffraction optics, we can also draw certain analytical conclusions about the aforementioned phenomena. Figure 5(a) shows that for a single diffraction fringe that is both bright and dark. We know that under multi-color illumination, the dual-phase grating interferometer can form two kinds of interference fringes with different peaks and the same direction in the detector plane, that is, the interference fringes are formed by ±1 level diffraction of the phase grating and the interference fringes are formed by −1 level and 0 level diffraction light (or +1 level and 0 level diffraction light).

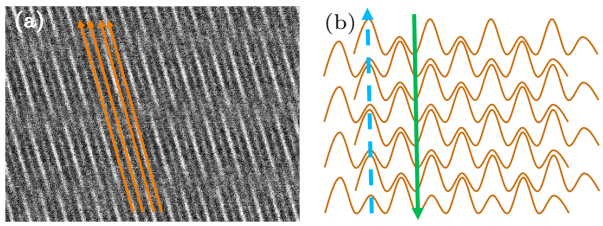


Fig. 5. Experimental results of three-phase grating and its fringe schematics.

The fringes that appear periodically along the orange arrow direction in Fig. 5(a) are the fringes with different peaks caused by the spectral distribution shown by the blue arrow (dashed line) in Fig. 5(b). The green arrow in Fig. 5(b) corresponds to the large-period moiré fringe. When a phase grating is introduced, each alternate diffracted light undergoes a π phase shift, which means that it becomes staggered by half a period.

5. Explanation of thin lens theory

Previous researches[18,29,30] indicate that the phase grating can be equivalent to a thin lens without considering its thickness. Next, we will present a simple method to calculate the period of multi-grating imaging fringes and set up the system parameters based on the thin lens imaging theory. For the standard Talbot–Lau interferometer,[19,31] fractional Talbot distance can be expressed as

$$f_1 = \frac{2l_1 + 1}{8}\frac{p_1^2}{\lambda}. \tag{16}$$

The fringe period can be expressed as

$$p_{\mathrm{f}} = \frac{d_1 + d_2}{d_1}\frac{p_1}{2}. \tag{17}$$

In previous study, it was assumed that there is a virtual imaging plane between G_1 grating and G_2 grating, which is named the 1st image. Using this virtual imaging plane as the intermediary, we can divide the multi-grating imaging system into multiple imaging systems based on a single grating, and use the thin lens imaging formula to perform simple and fast calculations. The flow charts are as follows.

Figure 6 shows that a three-grating imaging system is decomposed into three single grating systems (distinguished by the background color). Using three thin lens imaging formulas and a single-phase-grating-imaging fringe period formula, we can calculate all the system parameters and the input parameters necessary for each single grating system, ensuring that the image (img) contrast is maximized.

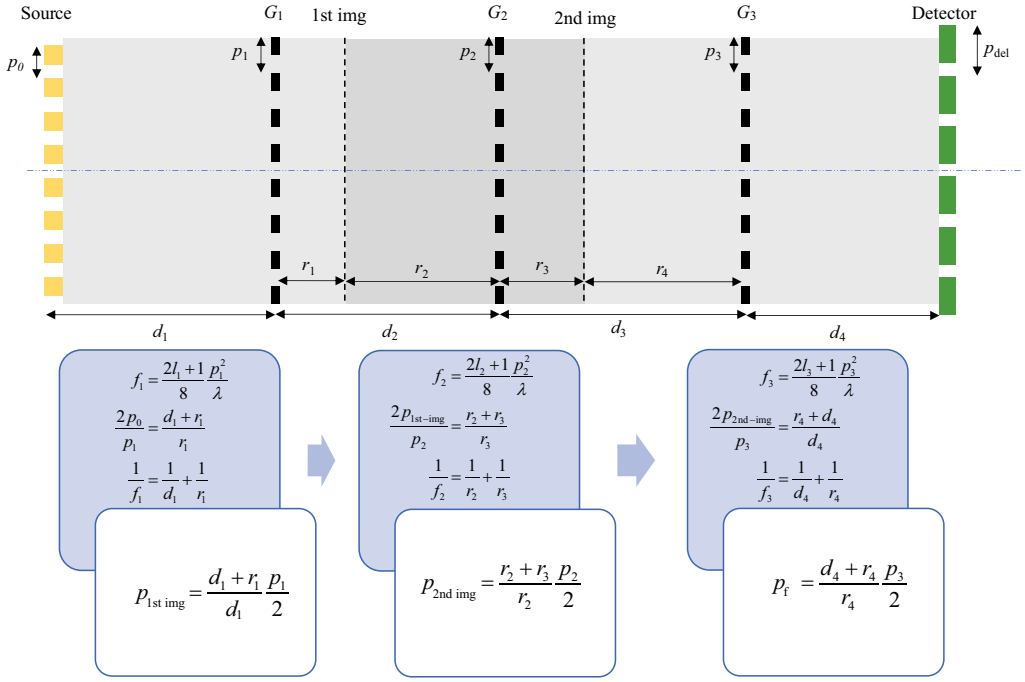


Fig. 6. Schematic diagram of three-or-multi-phase grating interferometer.

6. System design and simulation

Three-phase grating imaging systems have more design possibilities than dual-phase grating systems. We create three sets of three-grating imaging systems based on different grating periods and grating phase differences. The relevant parameters and simulation results are as follows.

Table 1. Design parameters of three-grating imaging system.

	λ (nm)	p_1 (μm)	p_2 (μm)	p_3(μm)	d_1 (cm)	d_2 (cm)	d_3 (cm)	d_4 (cm)	p_{f} (μm)
π–π–π	0.073	2.860	2.860	2.860	98.024	4.225	4.225	98.024	69.215
π–π–π	0.049	1.190	0.600	1.190	43.185	5.413	5.413	43.185	72.000
$\pi/2$–π–$\pi/2$	0.049	0.600	0.600	0.600	86.371	5.398	5.398	86.371	72.000

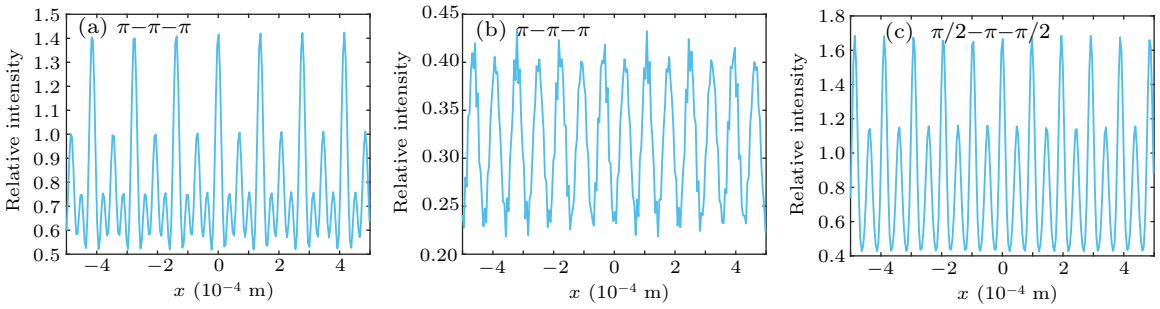


Fig. 7. Fringe images obtained by simulation using the data in the above table.

7. Conclusions

In this work, we provided a more complete theoretical formula for the imaging theory of a three-phase grating interferometer and verified it, systematically analyzing the relationship between three-phase grating interferometer and dual-phase grating interferometer. In terms of system design, a three-phase grating interferometer has only one more phase grating than a dual-phase grating interferometer. Therefore, there are many connections and similarities between the three-phase grating interferometer and the dual-phase grating interferometer, and under certain conditions, these two types of grating interferometers can be converted into each other. At the same time, because it does not need analyzing gratings, the three-phase grating interferometer has the advantages of easier grating fabrication and larger field of view. In addition, we

have experimentally demonstrated that the three-phase grating interferometer can easily produce millimeter-level moiré fringes, allowing it to be detected directly with clinical medical detectors.

Appendix A

The x-ray distribution on the front surface of G_2 grating can be expressed as

$$U_2(x_2) = \frac{1}{\sqrt{\mathrm{i}\lambda}} \int U_1^{'}(x_1) \frac{\exp(\mathrm{i}kr_2)}{d_2} \mathrm{d}x_1. \tag{A1}$$

Introduce the U_1' expression into Eq. (A1) and replace it with the standard form of the Fourier transform equation, then the resulting equation will be

$$U_2(x_2) = U_0 \sum_n a_n \frac{\exp[\mathrm{i}k(d_1+d_2)]}{\sqrt{d_1 d_2 (d_1+d_2)}} \exp\left[\frac{\mathrm{i}\pi}{\lambda}\left(\frac{x_\mathrm{s}^2}{d_1}+\frac{x_2^2}{d_2}\right)\right] \times \exp\left[-\mathrm{i}\pi\lambda \frac{d_1 d_2}{d_1+d_2}\left(\frac{x_\mathrm{s}}{\lambda d_1}-\frac{n}{p_1}+\frac{x_2}{\lambda d_2}\right)^2\right]. \tag{A2}$$

According to the complex amplitude distribution of the detector plane light field, the detector plane light intensity distribution can be expressed as

$$\begin{aligned} I(x_4) = {} & \frac{U_0^2}{d_1 d_2 d_3 d_4 L} \sum_{n'} \sum_{m'} \sum_{q'} \sum_{n'+s} \sum_{m'+r} \sum_{q'+t} a_{n'+s} b_{m'+r} h_{q'+t} a_{n'} b_{m'} h_{q'} \cdot \exp\left[\mathrm{i}2\pi \frac{x_4}{M_3}\left(\frac{s}{M_1 M_2 p_1}+\frac{r}{M_2 p_2}+\frac{t}{p_3}\right)\right] \\ & \times \exp\left[\mathrm{i}2\pi x_\mathrm{s}\left[\frac{d_2}{d_1+d_2}\frac{s}{p_1}+\frac{d_3}{d_1+d_2+d_3}\left(\frac{s}{M_1 p_1}+\frac{r}{p_2}\right)+\frac{d_4}{L}\left(\frac{s}{M_1 M_2 p_1}+\frac{r}{M_2 p_2}+\frac{t}{p_3}\right)\right]\right] \\ & \times \exp\left[\frac{-\mathrm{i}2\pi\lambda s(2n'+s)}{p_1^2} \times \frac{d_2 M_1 M_2^2 M_3 + d_3 M_2 M_3 + d_4 + d_3 M_1 M_2 M_3 \frac{p_1}{p_2}\frac{r}{s} + d_4 M_1 \frac{p_1}{p_2}\frac{r}{s} + d_4 M_1 M_2 \frac{p_1}{p_3}\frac{t}{s}}{2M_1^2 M_2^2 M_3}\right] \\ & \times \exp\left[\frac{-\mathrm{i}2\pi\lambda r(2m'+r)}{p_2^2} \times \frac{d_3 M_2 M_3 + d_4 + d_3 M_3 \frac{M_2}{M_1}\frac{p_2}{p_1}\frac{s}{r} + d_4 \frac{1}{M_1}\frac{p_2}{p_1}\frac{s}{r} + d_4 M_2 \frac{p_2}{p_3}\frac{t}{r}}{2M_2^2 M_3}\right] \\ & \times \exp\left[\frac{-\mathrm{i}2\pi\lambda t(2q'+t)}{p_3^2} \times \frac{d_4 + d_4 \frac{1}{M_1 M_2}\frac{p_3}{p_1}\frac{s}{t} + d_4 \frac{1}{M_2}\frac{p_3}{p_2}\frac{r}{t}}{2M_3}\right], \end{aligned} \tag{A3}$$

where $n = n'+s$, $m = m'+r$, and $q = q'+t$. Using the following equation:[32,33]

$$\sum_{l=-\infty}^{+\infty} C_l(d,\lambda,p_\mathrm{g},\Delta\phi_\mathrm{g}) = \sum_{l=-\infty}^{+\infty}\sum_{n=-\infty}^{+\infty} g_{l+n} g_n^* \exp\left(\frac{-\mathrm{i}2\pi l(l+2n)\lambda d}{2p_\mathrm{g}^2}\right) \tag{A4}$$

and after simplification, we can obtain

$$\begin{aligned} I(x_4) = {} & \frac{U_0^2}{d_1 d_2 d_3 d_4 L} \sum_s \sum_r \sum_t \exp\left[\mathrm{i}2\pi \frac{x_4}{M_3}\left(\frac{s}{M_1 M_2 p_1}+\frac{r}{M_2 p_2}+\frac{t}{p_3}\right)\right] \\ & \times \exp\left[\mathrm{i}2\pi x_\mathrm{s}\left[\frac{d_2}{d_1+d_2}\frac{s}{p_1}+\frac{d_3}{d_1+d_2+d_3}\left(\frac{s}{M_1 p_1}+\frac{r}{p_2}\right)+\frac{d_4}{L}\left(\frac{s}{M_1 M_2 p_1}+\frac{r}{M_2 p_2}+\frac{t}{p_3}\right)\right]\right] \\ & \times C_\mathrm{s}\left(\frac{d_2 M_1 M_2^2 M_3 + d_3 M_2 M_3 + d_4 + d_3 M_1 M_2 M_3 \frac{p_1}{p_2}\frac{r}{s} + d_4 M_1 \frac{p_1}{p_2}\frac{r}{s} + d_4 M_1 M_2 \frac{p_1}{p_3}\frac{t}{s}}{M_1^2 M_2^2 M_3}, \lambda, p_1, \phi_1\right) \\ & \times C_r\left(\frac{d_3 M_2 M_3 + d_4 + d_3 M_3 \frac{M_2}{M_1}\frac{p_2}{p_1}\frac{s}{r} + d_4 \frac{1}{M_1}\frac{p_2}{p_1}\frac{s}{r} + d_4 M_2 \frac{p_2}{p_3}\frac{t}{r}}{M_2^2 M_3}, \lambda, p_2, \phi_2\right) \\ & \times C_t\left(\frac{d_4 + d_4 \frac{1}{M_1 M_2}\frac{p_3}{p_1}\frac{s}{t} + d_4 \frac{1}{M_2}\frac{p_3}{p_2}\frac{r}{t}}{M_3}, \lambda, p_3, \phi_3\right). \end{aligned} \tag{A5}$$

Acknowledgements

Project supported by LingChuang Research Project of China National Nuclear Corporation and the National Natural Science Foundation of China (Grant No. 12027812).

References

[1] Miller J, Rochitte C, Dewey M, Arbab-Zadeh A, Niinuma H, Gottlieb I, Paul N, Clouse M, Shapiro E, Hoe J, Lardo A, Bush D, de Roos A, Cox C, Brinker J and Lima J 2008 *N. Engl. J. Med.* **359** 2324

[2] Zhang N and Zhu J F 2015 *International Journal on Smart Sensing and Intelligent Systems* **8** 45

[3] Fu J, Shi X H, Guo W and Peng P 2019 *Sci. Rep.* **9** 1113

[4] Kottler C, Pfeiffer F, Bunk O, Grünzweig C and David C 2007 *Rev. Sci. Instrum.* **78** 043710

[5] Teuffenbach MV, Koehler T, Fehringer A, Viermetz M, Brendel B, Herzen J, Proksa R, Rummeny EJ, Pfeiffer F and Noël P B 2017 *Sci. Rep.* **7** 7476

[6] Chamran F, Yeh Y T, Min H S, Dunn B and Kim C J 2007 *Journal of Microelectromechanical Systems* **16** 844

[7] Hyeon C, Kim D H, Kim K and Chun 2006 *J. Micromech. Microeng.* **16** 906

[8] Wehrspohn R, Schweizer S, Gesemann B, Pergande D, Geppert T, Moretton S and Lambrecht A 2013 *Comptes Rendus Chimie* **16** 51

[9] Bravin A, Coan P and Suortti P 2013 *Phys. Med. Biol.* **58** R1

[10] Sarapata A, Willner M, Walter M, Duttenhofer T, Kaiser K, Meyer P, Braun C, Fingerle A, Noël P, Pfeiffer F and Herzen J 2015 *Opt. Express* **23** 523

[11] Wang Z Y and Han B 2004 *Opt. Lett.* **29** 1671

[12] Bonse U and Hart M 1965 *Appl. Phys. Lett.* **6** 155

[13] Snigirev A, Snigireva I, Kohn V, Kuznetsov S and Schelokov I 1995 *Rev. Sci. Instrum.* **66** 5486

[14] Wiklins S W, Gureyev T, Gao D C, Pogany A and Stevenson A 1996 *Nature* **384** 335

[15] Ingal V N and Beliaevskaya E A 1995 *J. Phys. D: Appl. Phys.* **28** 2314

[16] Davis T, Gao D C, Gureyev T, Stevenson A and Wilkins S 1995 *Nature* **373** 595

[17] Chapman D, Thomlinson W, Johnston R, Washburn D, Pisano E, Gmür N, Zhong Z, Menk R, Arfelli F and Sayers D 1997 *Phys. Med. Biol.* **42** 2015

[18] David C, Nöhammer B, Solak H and Ziegler E 2002 *Appl. Phys. Lett.* **81** 3287

[19] Momose A, Kawamoto S, Koyama I, Hamaishi Y, Takai K and Suzuki Y 2003 *Jpn. J. Appl. Phys.* **42** L866

[20] Olivo A and Speller R 2007 *Phys. Med. Biol.* **52** 6555

[21] Talbot H F 1836 *The London, Edinburgh, and Dublin Philosophical Magazine and Journal of Science* **9** 401

[22] Miao H X, Panna A, Gomella A, Bennett E, Znati S, Chen L and Wen H 2016 *Nat. Phys.* **12** 830

[23] Lord Rayleigh F R S 1874 *Philosophical Magazine Series* **47** 81

[24] Kendig K 1980 *Pacific Journal of Mathematics* **89** 327

[25] Zhou S L, Fu Y Q, Tang X P, Hu S, Chen W F and Yang Y 2008 *Opt. Express* **16** 7869

[26] Yang J, Huang J H, Shan Y Z, Lei Y H, Zong F K and Guo J C 2023 *Acta Photon. Sin.* **52** 0105001

[27] Sarenac D, Pushin D, Huber M, Hussey D, Miao H X, Arif M, Cory D, Cronin A, Heacock B, Jacobson D, LaManna J and Wen H 2017 *Phys. Rev. Lett.* **120** 113201

[28] Yan A M, Wu X Z and Liu H 2020 *OSA Contin.* **3** 2782

[29] Kagias M, Wang Z T, Jefimovs K and Stampanoni M 2017 *Appl. Phys. Lett.* **110** 014105

[30] Lei Y H, Liu X, Huang J H, Du Y, Guo J C, Zhao Z G and Li J 2018 *J. Phys. D: Appl. Phys.* **51** 385302

[31] Guigay J P 2010 *Optica Acta* **18** 677

[32] Yan A M, Wu X Z and Liu H 2015 *Med. Phys.* **42** 3036

[33] Yan A M, Wu X Z and Liu H 2016 *Opt. Express* **24** 15927